MNRAS **000**, 1–20 (2015) Preprint 19 May 2016 Compiled using MNRAS LATEX style file v3.0

The rotation of the halo of NGC 6822 from the radial velocities of carbon stars

Graham P. Thompson,[1⋆] Sean G. Ryan,[1] Lisette F. Sibbons[1]
[1]*School of Physics, Astronomy and Mathematics, University of Hertfordshire, College Lane, Hatfield AL10 9AB, UK*

arXiv:1605.05582v1 [astro-ph.GA] 18 May 2016

Accepted XXX. Received YYY; in original form ZZZ

ABSTRACT

Using spectra taken with the AAOmega spectrograph, we measure the radial velocities of over 100 stars, many of which are intermediate age carbon stars, in the direction of the dwarf irregular galaxy NGC 6822. Kinematic analysis suggests that the carbon stars in the sample are associated with NGC 6822, and estimates of its radial velocity and galactic rotation are made from a star-by-star analysis of its carbon star population. We calculate a heliocentric radial velocity for NGC 6822 of -51 ± 3 km s^{-1} and show that the population rotates with a mean rotation speed of 11.2 ± 2.1 km s^{-1} at a mean distance of 1.1 kpc from the galactic centre, about a rotation axis with a position angle of $26^\circ \pm 13^\circ$, as projected on the sky. This is close to the rotation axis of the HI gas disk and suggests that NGC 6822 is not a polar ring galaxy, but is dynamically closer to a late type galaxy. However, the rotation axis is not aligned with the minor axis of the AGB isodensity profiles and this remains a mystery.

Key words: techniques: radial velocities – stars:AGB and post-AGB – galaxies:individual:NGC 6822 – galaxies: kinematics and dynamics – Local Group – infrared:stars

1 INTRODUCTION

NGC 6822 (Barnard's galaxy) is a relatively bright and well studied dwarf irregular galaxy. It lies within the Local Group (LG), quite close to the Milky Way, and is the third nearest dwarf irregular galaxy after the Large and Small Magellanic Clouds. It was the first object to be shown to lie outside the Milky Way by Edwin Hubble (Hubble 1925). It has no known close companions and lies in a region relatively devoid of other galaxies (de Blok & Walter 2000). Despite its apparent isolation, there is some evidence of tidal interaction and a burst of star formation 100 – 200 Myr ago (de Blok & Walter (2000) and references therein).

The location of NGC 6822 has a range of published values for right ascension (α) and declination (δ)[1], but for the purposes of this paper we use $\alpha = 19^{\rm h}44^{\rm m}56^{\rm s}$, $\delta = -14^\circ 48' 06''$ (J2000). This is at the centre of a 3 deg^2 field used by Sibbons et al. (2012, 2015) and is adopted here for consistency, since this study uses spectra drawn from their sample.

The galactic distance is variously reported to lie between 450 to over 500 kpc. For the purposes of this paper, its distance is not important, but where we do use it, we again adopt the same value as Sibbons et al. (2012, 2015), 490 ± 40 kpc, for consistency with that work. This is the value quoted in Mateo (1998). Sibbons et al. (2012, 2015) also quotes a distance modulus for NGC 6822 of $(m-M)_0 = 23.45 \pm 0.15$ ($\approx 490 \pm 34$ kpc). In recent years, papers have been published which have provided new distance moduli using Cepheid variables. Many of these re-estimates have reduced the radial distance to NGC 6822 by about 10% from the value used herein. The distance modulus derived by Gieren et al. (2006) is $(m-M)_0 = 23.312 \pm 0.021$ ($\approx 460 \pm 4.4$ kpc), Feast et al. (2012) gives $(m-M)_0 = 23.40 \pm 0.05$[2] ($\approx 479 \pm 11$ kpc), and Rich et al. (2014) gives $(m-M)_0 = 23.38 \pm 0.02_{\rm stat} \pm 0.04_{\rm sys}$ ($\approx 474 \pm 13_{\rm tot}$ kpc). In Whitelock et al. (2013), an alternative to Cepheid variables is proposed using Mira variables for distance measurement. These are AGBs which vary in magnitude over periods of several hundred days. NGC 6822 is used as one example of the measurement of distance using Mira variables and after calibration of the method using Miras in the Large Magellanic Cloud, the distance module for NGC 6822 is given

⋆ E-mail: g.p.thompson@herts.ac.uk

[1] SIMBAD: $\alpha = 19^{\rm h}44^{\rm m}56.199^{\rm s}$, $\delta = -14^\circ 47' 51.29''$ (J2000).
NED: $\alpha = 19^{\rm h}44^{\rm m}57.7^{\rm s}$, $\delta = -14^\circ 48' 12''$ (J2000).
McConnachie (2012): $\alpha = 19^{\rm h}44^{\rm m}56.6^{\rm s}$, $\delta = -14^\circ 47' 21''$ (J2000).

[2] Feast et al. (2012) does not claim any precision with the error value, owing to the difficulty in measuring the true uncertainty in the value of the distance modulus.

© 2015 The Authors

as $(m-M)_0 = 23.56 \pm 0.03$ mag ($\approx 515 \pm 7$ kpc), somewhat greater than the other estimates.

Morphologically, NGC 6822 has three components: a gaseous disk of HI (Fig. 1, left hand panel), an outer spheroid of stars (Fig. 1, right hand panel) and a small central core of young stars (Hodge et al. 1991). Its HI content has been studied by de Blok & Walter (2000) and its the stellar content, especially Red Giant Branch (RGB) and Asymptotic Giant Branch (AGB) stars, by Letarte et al. (2002), Battinelli et al. (2006), Demers et al. (2006) and Sibbons et al. (2012, 2015). The HI gas disk appears to lie at a position angle (PA) of $\sim 130^\circ$ when observed from tip to tip (de Blok & Walter 2000). However, it also appears to twist and in Weldrake et al. (2003), the PA is stated as $\sim 110^\circ$, which is closer to the major axis of the central part of the disk, as shown in Fig. 1 (left hand panel). Letarte et al. (2002) shows that carbon stars lie well outside the HI disc and Demers et al. (2006) and Battinelli et al. (2006) show that the isophotes of RGBs of NGC 6822 are also elliptical, where the major axis PA changes from $\sim 65^\circ$ (outermost contour) to $\sim 80^\circ$ (innermost contour), as shown in Fig. 1 (right hand panel).

Much of the published velocity data for NGC 6822 has been derived from the HI gas content of NGC 6822 using the 21 cm line (Koribalski et al. 2004; Weldrake et al. 2003). Koribalski et al. (2004) measures a heliocentric radial velocity, $V_{\rm helio}$, of -57 ± 2 km s^{-1} for NGC 6822 from its HIPASS spectrum, and this now a commonly cited value. Mateo (1998), and sources therein, also provide $V_{\rm helio}$ based on the HI component, $V_{\odot,\rm radio}$ of -54 ± 6 km s^{-1}, and Weldrake et al. (2003) similarly provides a HI derived systemic (radial) velocity[3] in the range -53.3 km s^{-1} to -54.7 km s^{-1} at the centre of the HI gas.

Rotation of the gas disk has also been measured at 21 cm. Mateo (1998) provides a value for the rotation of the HI disk, $v_{\rm rot,ISM}$, of 47 ± 3 km s^{-1}, and Weldrake et al. (2003) shows that the velocity of the HI disk ranges from -100 km s^{-1} at the NW extreme (blue-shifted) to $+10$ km s^{-1} at the SE extreme (red-shifted). McConnachie (2012) quotes a peak observed rotation speed of 47 ± 2.0 km s^{-1}, uncorrected for inclination or asymmetric drift, citing Koribalski et al. (2004); Weldrake et al. (2003).

With regard to the stellar kinematics of NGC 6822, Mateo (1998), and references therein, provide a value of $V_{\rm helio}$ based on optical measurements of $V_{\odot,\rm opt} = -53 \pm 4$ km s^{-1}. Kirby et al. (2014) studies the kinematics of seven isolated dwarf galaxies in the LG from the radial velocities of red giant stars, including NGC 6822, and derives a mean heliocentric radial velocity, $\langle V_{\rm helio} \rangle$, of -54.5 ± 1.7 km s^{-1}for NGC 6822.

However, while there are published data for $V_{\rm helio}$, there are little regarding stellar rotation. Many publications refer to Demers et al. (2006) for stellar rotation, where the radial velocities for 110 carbon stars lying within $15'$ (~ 2.1 kpc) of the HI major axis, taken from a sample in Letarte et al. (2002), are measured, although the individual stellar measurements are not published. A variation in residual velocity along the major axis of the outermost RGB isophote is interpreted to be a signature of rotation about the minor axis. As a result, the paper suggests that the carbon stars appear to rotate about an axis roughly perpendicular to the rotation axis of the HI disk, resembling a Polar Ring Galaxy (PRG). It would be extraordinarily useful if NGC 6822 is a PRG, since they are very rare. The Sloan Polar-Ring Catalogue (SPRC), which uses images from the Sloan Digital Sky Survey, includes only 6 confirmed PRGs from a total of just 275 candidates. Discovery of a nearby PRG would present a remarkable opportunity to study these galactic types at close hand. In a separate publication (Demers & Battinelli 2007) suggest that radial velocities of individual NGC 6822 giants might give some insight into rotation of the stellar population.

Kirby et al. (2014) checked for signs of rotation in their sample of 7 dwarf galaxies, and found that only the Pegasus dwarf irregular showed obvious signs. For NGC 6822, they refer to the findings of Demers et al. (2006). They comment that while a rotation of the order of ~ 10 km s^{-1} is possible in NGC 6822, their data were too highly obscured by velocity dispersions to be certain.

The published studies of the galaxy's stellar rotation are complemented by other studies of the motion of globular clusters (Veljanoski et al. 2015) and planetary nebulae (Flores-Durán et al. 2014). Veljanoski et al. (2015) studies the globular cluster (GC) system of NGC 6822, in which 8 GCs are presently identified (see Table 1 therein). The radial velocities of 6 of the GCs are given and $\langle V_{\rm helio} \rangle$ is deduced to be between -59 and -60 km s^{-1}. The spatial distribution of the GCs in their data is rather linear and lies approximately parallel to the major axis of the AGB isophotes. Three possible dynamical models are considered:

- 'Disk model', in which the rotation axes are similar to that suggested by Demers et al. (2006). The resulting rotation rate is 12 ± 10 km s^{-1}.
- 'Cigar model', where the cluster system shares the same rotation axis as the HI disk. In this case the rotation rate is determined to be 56 ± 31 km s^{-1}.
- A scenario where there is no net rotation by disconnecting any relationship between the gas disk and the stellar component.

In none of these models are they able to independently determine the PA of the rotation axis owing to the small number of objects in their sample of GCs, but their preferred case is the 'Disk model', owing to its low rotation rate. They argue that in the case of the 'Cigar model' the rotation is too high, and would cause the sample to flatten into a disk which they do not observe.

In Flores-Durán et al. (2014), the motion of 10 planetary nebulae (PNe) in the galaxy are studied. PNe are the evolutionary stage reached by AGBs after the end of their lives, and may thus provide complementary kinematic information of the galaxy. Flores-Durán et al. (2014) compute the mean $\langle V_{\rm helio} \rangle$ of the PNe to be -57.8 km s^{-1}. They compare their result with four extended star clusters (ESGs) which have a mean $V_{\rm helio}$ of -88.3 km s^{-1} (Hwang et al. 2014) and with a C-star mean $V_{\rm helio}$ of -32.9 km s^{-1} derived by Hwang et al. (2014). The ESGs lie ~ 10.5 kpc from the centre of NGC 6822 and show no signs of rotation (Hwang et al. 2014). Flores-Durán et al. (2014) infer that the PNe, C-stars and clusters belong to different dynamical systems, but with

[3] We assume all velocities quoted in Weldrake et al. (2003) are corrected to heliocentric

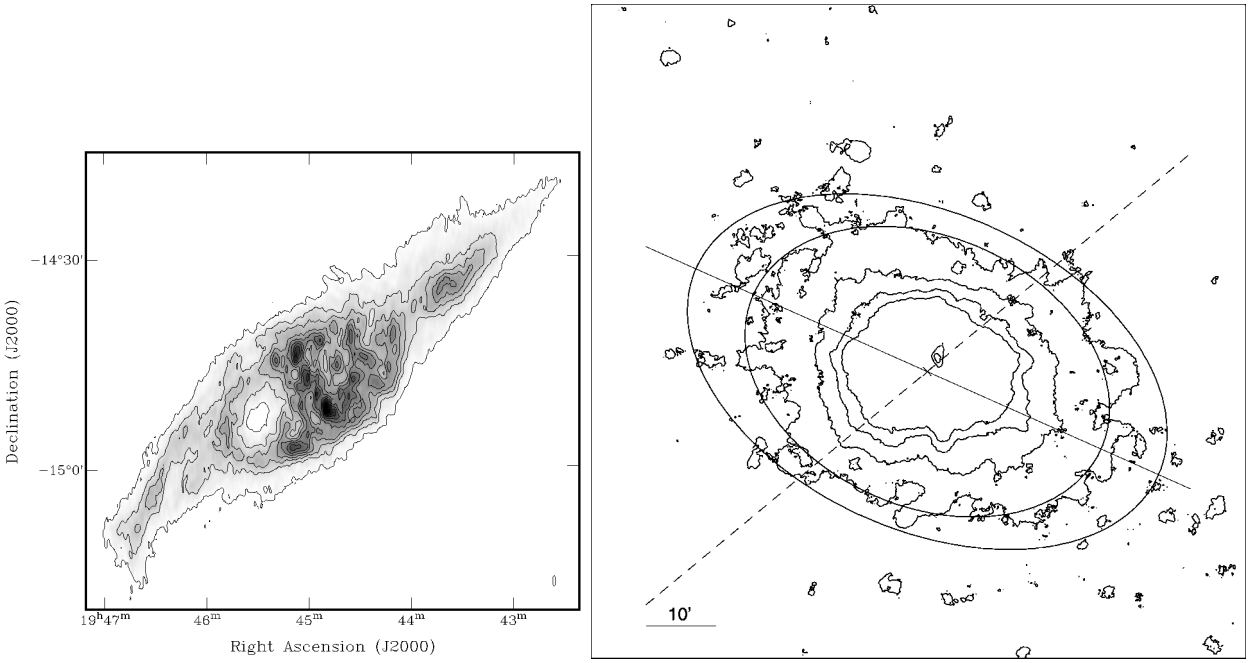

Figure 1. Left hand panel, HI isodensity curves of NGC 6822 (de Blok & Walter 2000). The HI curves exhibit a disk-like structure, which is twisted with a major axis *PA* from $\sim 110°$ to $\sim 130°$. Right hand panel, RGB stellar isodensity profiles (Demers et al. 2006). The RGB profiles exhibit elliptical contours, where the major axis *PA* changes from $\sim 65°$ (outermost contour) to $\sim 80°$ (innermost contour). The solid line in the right hand panel lies at 65° and the dashed line lies 130°. The panels are shown to approximately the same scale and orientation.

so few PNe, they are unable to reliably fit the radial velocity data to either system.

This paper provides the results of a new study of the kinematics of NGC 6822, based on the spectra of individual stars obtained in 2011 by Sibbons et al. (2015), and follows studies by Sibbons et al. (2012, 2015) which classify stars, photometrically and spectroscopically, from a set taken from the catalogue of Letarte et al. (2002). These studies were able to distinguish C-type and M-type AGBs from other types, so that although Demers & Battinelli (2007) cautions that the separation of carbon stars associated with NGC 6822 from foreground Galactic dwarfs might be difficult, our present study has the advantage of using the spectra of stars which have already been classified as carbon stars in NGC 6822, with a high degree of confidence.

The radial velocities of well over 100 stars within a 4 kpc radius of the centre of NGC 6822, (the *inner region*), and well over 100 stars outside the 4 kpc radius, (the *outer region*), are measured and reported. In the inner region many of these stars are classified as carbon stars and are expected to be associated with the galaxy (Sibbons et al. 2015). In the outer region, most of the stars are expected to be foreground Milky Way stars (Sibbons et al. 2012, 2015).

Based on the aggregated sample of carbon stars in the inner region, a value for the heliocentric radial velocity of NGC 6822 is derived. The kinematics of individual stars in the sample indicate that they belong to the same population, supporting Sibbons et al. (2015). Moreover, the radial velocity measurements are accurate enough to reveal rotation of the stellar component about an axis through the centre of the galaxy, and to derive its rotational speed and a new *PA* for the axis of rotation. In §2, we discuss the data set, its origins and its limitations. In §3, we discuss the method used to analyse the data set including the selection of objects for analysis. In §4, we discuss the results and in §5, we draw conclusions.

2 OBSERVATIONS AND DATA

This study uses AGB stars as tracers of kinematic properties of the galaxy. AGB stars are amongst the brightest stars in an intermediate-age or old stellar population and can be resolved in galaxies beyond the Milky Way, making it possible to study them individually. AGBs tend to divide into those with oxygen rich atmospheres (M-types), and those with carbon rich atmospheres (C-types or carbon stars). They have relatively low surface temperatures, $T_{\rm eff}$, ranging from as low as 2200 K (Matthews et al. 2015) for old stars near the end of their lives up to ~ 4000 K for intermediate age stars[4]. The continuum peaks at wavelengths in the near infra red, with increasing brightness through the *I*, *J*, *H* and *K* bands.

The spectrum of a typical AGB contains a number of absorption features, predominantly broad TiO bands in M-type AGBs, broad CN bands in C-type AGBs. The *I*−band spectral region also contains the Ca II triplet lines in both types of AGB. The Ca II triplet lines are ideal for measuring radial velocities as they are narrow atomic features and lie in a position where the continuum is relatively strong. In this study, we use the spectra of carbon rich AGBs classified by

[4] In van Belle et al. (2013), 12 carbon stars are found to be in a range of $T_{\rm eff} = 2381 \pm 81$ K to 3884 ± 161 K, with a mean at 2800 ± 270 K.

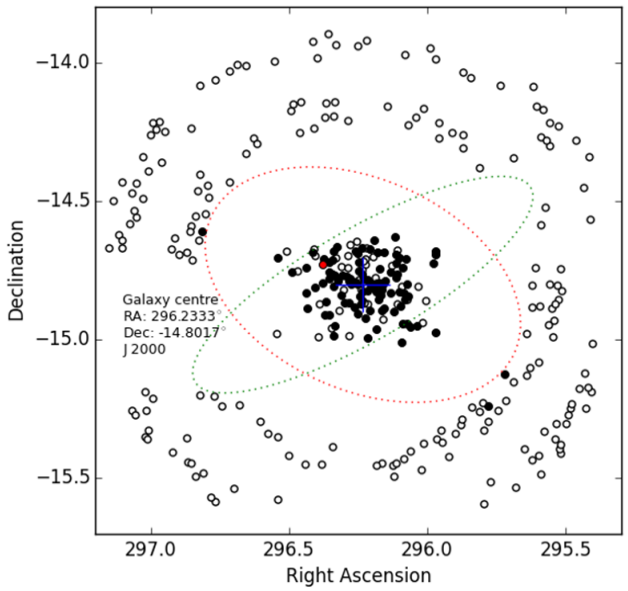

Figure 2. The locations of 323 NGC 6822 objects targeted by Sibbons et al. (2015), shown over 1.8° of the sky. The black points and red point show 99 objects classified by Sibbons et al. (2015) as C-type AGBs. The red point marks object #31, which is discussed in the text. The 3 outermost C-type AGBs lie more than 4 kpc from the galactic centre and were not used in the analysis. The open circles mark the remaining objects which are given other classifications. The dotted ellipses approximate the location and extent of the gas disk and outermost stellar isodensity profile shown in Fig. 1. The concentric appearance of the outer objects is due to the layout of the fibres on the spectrograph field plate.

Sibbons et al. (2015) as follows: confirmed C-type stars (C); tentative C-type stars (C:), confirmed C-type stars which exhibit Hα and sometimes [S II] and [N II] emission (Ce) and tentative C-type stars which similarly exhibit emission (Ce:).

Wide band, low resolution spectra for 323 target objects, out to ≈ 8 kpc from the galactic centre, were obtained using the AAOmega multi-fibre spectrograph on 30 and 31 August 2011 (Sibbons et al. 2015). An optical fibre was placed over each target object position on the field plate of the spectrograph and throughout this paper, objects are referred to by their fibre number. Wide band gratings 385R and 580V were used in the spectroscopy but this study uses only the spectra from grating 385R, which has a bandpass from 5687 Å to 8856 Å, covering the Ca II triplet, dispersed at 1.6 Å pixel^{-1}. The spectra were reduced to science frames, using the AAOmega pipeline. The spatial position of each object is plotted in Fig. 2, which shows 135 objects in the inner region, and 188 objects in the outer region. Ninety eight black points and one red point show the positions of the C-type AGBs. The red point is the location of object #31 which was utilised in the processing of the data described later. Three black points located just outside the outermost isodensity profile were not used in the analysis, so the total number of carbon stars used is 96. Ellipses which reproduce the location and extent of the gas disk and outermost RGB isodensity profile of NGC 6822 are also plotted on Fig. 2.

Fig. 3 shows the spectra of a typical C-type AGB, object #31, for both observing nights. It is evident that the spectrum of 31 August has a higher count in the continuum than that of 30 August and this results in a correspondingly higher signal to noise ratio, *SNR*. This is generally the case for all spectra and led us to place more weight on the results for the night of 31 August. The waveband containing the Ca II triplet is shaded in grey in the left hand panel and its absorption features indicated at 8498.02 Å, 8542.09 Å and 8662.14 Å (rest) in the right hand panel.

Although the velocity resolution of the grating was rather low, ≈ 56 km s^{-1} pixel^{-1} in the Ca II triplet waveband of interest, and the individual errors rather higher, there were enough stars present in the sample to reduce the standard error in the mean velocity to $\sim 8\%$.

3 RADIAL VELOCITY MEASUREMENTS

To measure relative velocities, we used the cross-correlation technique of Tonry & Davis (1979), as implemented in the IRAF[5] routine *fxcor*, star by star. We produced two composite spectra from the spectra of the AGBs in the sample, which were used as the template required by this technique. One template was made from C-type AGBs from the inner region, and the second from the dM-type stars in the outer region as classified by Sibbons et al. (2015). Both templates were corrected to the 'rest frame', and then used to measure the radial velocities of the stars. The C-type template was used for all stars, while the M-type template was used for the objects in the outer region only.

The use of a composite template ensures that its spectrum is well matched to the object spectra, that is, it includes the same instrument and observing systematics as the object spectra. Moreover, the combination process makes a significant reduction in the noise content in the template, an important consideration as our spectra had originally been taken with a relatively short exposure time. The composite template spectra are shown in Fig. 4. The undulations in the C-type spectrum are due to the remaining Ca II triplet and to CN absorption lines.

fxcor generates a cross-correlation function of an object spectrum and the template spectrum, and fits a Gaussian to it. As the template is in the rest frame, the position of the Gaussian peak with respect to the baseline determines the radial velocity, V_r, of the object, and application of the heliocentric correction[6] yields an object's heliocentric radial velocity, $V_{\rm helio}$. Initial experimentation and visual inspection were performed to find the best parameters to use in *fxcor* to minimise errors and maximise the number of successful cross-correlation operations. It was found that a 9 pixel Gaussian fit ($\equiv$ 13.5 Å or 717 km s^{-1}) fitted the shape of the peak of the cross-correlation function closely and did not limit the number of successful cross-correlations. All spectra were truncated to the waveband 8440 Å to 8710 Å, which covers the Ca II triplet, to ensure that IRAF calculated the

[5] IRAF is distributed by the National Optical Astronomy Observatory, which is operated by the Association of Universities for Research in Astronomy (AURA) under a cooperative agreement with the National Science Foundation.

[6] -19.5 km s^{-1} (30 August 2011) and -19.8 km s^{-1} (31 August 2011)

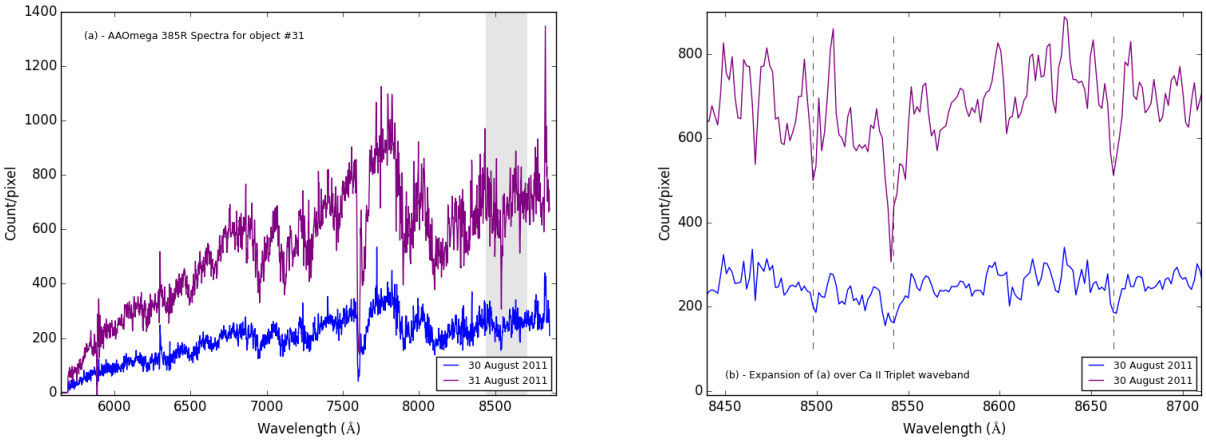
(a) - AAOmega 385R Spectra for object #31
Count/pixel
Wavelength (Å)
30 August 2011
31 August 2011
(b) - Expansion of (a) over Ca II Triplet waveband
30 August 2011
30 August 2011

Figure 3. Spectra for Object #31. Left hand panel: Full red spectrum from AAOmega grating 385R for object # 31 on 30 and 31 August 2011. Object #31 is spectrally classified as a C-type star in Sibbons et al. (2015) and has CN absorption bands at 5730, 6206, 6332, 6478, 6631, 6925, 7088, 7259, 7437, 7876, 8026 Å which are characteristic of this type of star. The large absorption feature at 7594 Å is due to telluric O_2. The grey band indicates the waveband 8440Å to 8710Å containing the Ca II triplet features. Right hand Panel: The same spectra expanded over the waveband 8440Å to 8710Å containing the Ca II triplet features used for radial velocity measurement. The centres of the Ca II triplet absorption lines are indicated by the vertical dashed lines at 8498.02 Å, 8542.09 Å, 8662.14 Å.

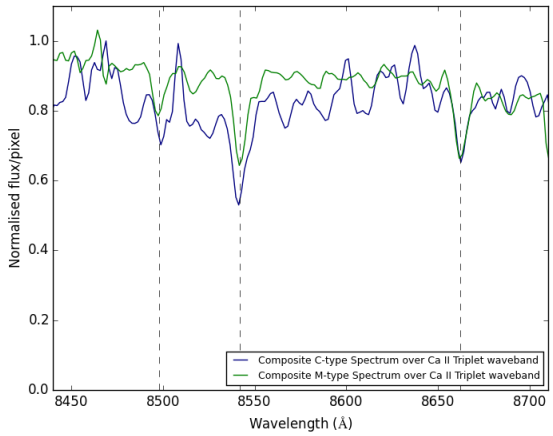
Normalised flux/pixel
Wavelength (Å)
Composite C-type Spectrum over Ca II Triplet waveband
Composite M-type Spectrum over Ca II Triplet waveband

Figure 4. Composite template spectra in the rest frame used for the radial velocity measurements. The centres of Ca II triplet features are shown by the vertical dashed lines.

velocity resolution appropriate to this waveband, and the cross-correlation bandwidth was restricted to 8450 Å to 8700 Å to reduce spectral noise coming from outside this waveband.

The quality of the spectra is important. As well as low spectral resolution, many of our spectra had low *SNR* (< 10 pixel^{-1}), causing noisy cross-correlation functions. These sometimes returned unreliable results or failed to give a result at all. To overcome these difficulties, selection criteria were adopted to rule out any spectra which might give rise to unreliable results. The criteria were based on the strength of the cross-correlation function, *hght* and on the radial velocities returned by *fxcor* as described below.

It was found, by inspection, that cross-correlation functions with $hght > 0.4$ give a strong peak with low sidebands, but those with $hght < 0.2$ do not. In these cases, the peaks are weak with respect to the sidebands and in some cases, multiple peaks occur. Between these limits, the quality of the cross-correlations degrades but useful results can be achieved in many cases. After visual inspection of each cross-correlation function, we excluded all cross-correlation functions where $hght < 0.2$.

We then examined the *fxcor* velocity returns. In a number of cases, unrealistically high values of $V_{\rm helio}$ were observed. These can come about by selection of the 'wrong' peak by *fxcor* in noisy or multi-peak cross-correlation functions. Values of $V_{\rm helio}$ as large as $\pm$1554 km s^{-1}, $\pm$4184 km s^{-1} or $\pm$5734 km s^{-1} arise, which are regarded as unrealistic, and such values tend to be associated with *hght* values close to or less than 0.2. The distribution of velocities returned from *fxcor*, corrected to $V_{\rm helio}$, was analysed and showed that most velocities fall within $\pm$200 km s^{-1}. All cross-correlation functions where $hght > 0.4$ yielded velocities within this range so, on this basis, heliocentric velocities falling outside this range were excluded.

Table 1. The first 18 lines of the individual results for objects meeting the criteria ($hght \geqslant 0.2$, -200 km s^{-1} $\leqslant V_{\rm helio} \leqslant +200$ km s^{-1}). The full table can be found in Appendix A1 to the electronic version of this paper

Objects meeting the criteria ($hght \geqslant 0.2$, -200 km s^{-1} $\leqslant V_{\rm helio} \leqslant +200$ km s^{-1}).																
[1]	[2]	[3]	[4]	[5]	[6]	[7]	[8]	[9]	[10]	[11]	[12]	[13]	[14]	[15]	[16]	[17]
									30 August 2011				31 August 2011			
#Fibre	ID	RA (°)	Dec (°)	I−band (mag.)	distance (kpc)	phot. class.	spec. class.	*SNR*	*hght*	$V_{\rm helio}$ (km s^{-1})	$V_{\rm err}$ (km s^{-1})	*SNR*	*hght*	$V_{\rm helio}$ (km s^{-1})	$V_{\rm err}$ (km s^{-1})	Flag
1	217716	296.23	-14.86	19.3	0.52	M	Ce:	7	0.39	-10	49	9	0.48	-35	36	C
2	239630	296.33	-14.95	19.4	1.52	C*	C:	6	0.43	-55	41	7	0.54	-55	27	C
3	210316	296.43	-14.83	18.9	1.69	M	C:	5	0.59	15	25	6	0.76	-11	16	C
4	174035	296.37	-14.71	19.1	1.4	M*	C	3	0.37	-26	57	5	0.27	-43	67	C
6	199974	296.37	-14.8	19.2	1.17	M	C	...	...	...	...	9	0.65	4	24	C
7	194949	296.35	-14.78	18.9	1	C*	C:	12	0.72	-1	34	18	0.75	-14	23	C
8	242030	296.35	-14.96	18.8	1.64	...	...	6	0.6	-53	21	9	0.7	-62	22	...
9	220271	296.39	-14.87	...	1.43	...	...	5	0.48	-28	40	8	0.59	-63	27	...
10	188246	296.49	-14.76	18.3	2.12	M	C:	6	0.57	-40	29	10	0.8	-39	16	C
11	172656	296.54	-14.71	19.3	2.66	C*	C	5	0.29	-125	69	8	0.39	-70	41	C
12	211898	296.31	-14.84	18.8	0.7	M	C	9	0.57	-31	26	7	0.74	-21	20	C
14	246838	296.54	-14.98	...	2.99	...	...	4	0.36	-78	37	5	0.57	-61	28	...
15	206867	296.3	-14.82	...	0.59	...	...	7	0.42	1	58	8	0.42	-3	38	...
17	225812	296.32	-14.9	...	1.06	...	...	4	0.33	0	75	6	0.51	-10	31	...
18	190283	296.34	-14.76	19.6	0.96	M	C	6	0.45	-44	33	5	0.36	-51	36	C
19	168284	296.41	-14.69	19.0	1.78	C*	C:	9	0.48	40	42	10	0.48	21	34	C
21	213379	296.24	-14.85	19.9	0.39	C*	Ce:	4	0.4	-25	42	...	...	...	...	C
22	200573	296.27	-14.8	19.0	0.34	M	Ce	8	0.37	10	73	9	0.72	-12	17	C

Column

1 & 2 — Fibre number and the target identifier respectively as defined by Sibbons et al. (2015).

3 & 4 — Right ascension (RA) and declination (Dec) of each object (J2000) according to Sibbons et al. (2015).

5 — I−band magnitude of C-type AGBs in the inner region from the catalogue of Letarte et al. (2002).

6 — Distance of the object from the putative galactic centre ($\alpha = 19^h:44^m:56^s$ (296.2333°), J2000 and $\delta = -14°:48':06''$ (−14.8017°), J2000) centred on the optical co-ordinates of NGC 6822[7] adopted by Sibbons et al. (2012, 2015) and a galactic distance of 490 kpc (Mateo 1998).

7 & 8 — Photometric classification of each object from Sibbons et al. (2012), and its corresponding spectroscopic classification from Sibbons et al. (2015).

9 & 13 — *SNR* of each object calculated in the band 8560 Å to 8650 Å for the nights of 30 August 2011 and 31 August 2011 respectively.

10, 11 & 12 — *hght*, the heliocentric radial velocity ($V_{\rm helio}$) and the velocity error ($V_{\rm err}$) returned from *fxcor* for the night of 30 August 2011.

14, 15 & 16 — *hght*, the heliocentric radial velocity ($V_{\rm helio}$) and the velocity error ($V_{\rm err}$) returned from *fxcor* for the night of 31 August 2011.

17 — Flag showing which objects were used in the composite templates: "C" for the C-type composite and "M" for the M-type composite.

4 RESULTS AND ANALYSIS

4.1 Cross-correlation results with the C-type template

All 323 objects were cross-correlated with the C-type composite template. Application of the criteria discussed in §3 resulted in 128 successful cross correlations in the inner region and 107 in the outer region on 30 August, and 129 in the inner region and 124 in the outer region on 31 August. From the population of 96 C-type AGBs in the inner region, 89 gave results meeting the selection criteria on 30 August and 92 on 31 August.

The full results of the radial velocity measurements and their individual errors over both nights are shown in full in the Appendix to the electronic version of this paper. The first 18 lines of these results are reproduced in Table 1, with explanations of the column contents. Spectra which failed to meet the selection criteria are not included.

Table 2 summarises the results. Column [3] shows the mean heliocentric radial velocities, $\langle V_{\rm helio}\rangle$, of the sample. For the inner region, this can be considered a good approximation to the heliocentric radial velocity of NGC 6822. The mean individual error in column [4] is large and reflects the low resolution and low *SNR* of the spectra. $\sigma(V_{\rm helio})$ in Column [5], is the velocity dispersion, which is also high, nevertheless, the standard error of the mean (SE) in column [6] is small, $3-8$ km s^{-1}, implying that, provided the individual errors are random, the mean and median (column [7]) heliocentric radial velocities are well constrained. The mean velocities show reasonable consistency from night to night, with differences similar to the standard error in the mean, SE. The inner region differs by > -24 km s^{-1} from the outer region[8], supporting the suggestion that the objects in the outer region are not part of NGC 6822.

Thus, we conclude that the heliocentric radial velocity of NGC 6822, as based on the sample of the inner C-type AGB population, lies in the median range of -43 ± 4 to -51 ± 3 km s^{-1} (1σ). The data for 31 August are preferred, owing to their better *SNR*, lower errors and greater number of successful cross-correlations than the data for 30 August, and provides $V_{\rm helio}= -51\pm3$ km s^{-1} (1σ). This compares favourably with published values described earlier.

Fig. 5 plots $V_{\rm helio}$ of all objects which meet the acceptance criteria, by distance D from the galactic centre, for both nights. It shows a number of differences between the inner and outer populations. The inner objects tend to clump more closely around the median value for the inner region and they are therefore likely to be part of the same dynamical system, while the outer objects are much more widely spread about a different median value, indicating a separate population. This suggests that the inner population is associated with NGC 6822, supporting similar conclusions in Sibbons et al. (2012, 2015), while the outer population is not.

The aggregated results of the cross-correlation of the spectra of objects in the outer region using the M-type template are also presented in Table 2. Both the formal errors, $\langle V_{\rm err}\rangle$, and the spread of results, $\sigma(V_{\rm helio})$, are reduced by switching to the M-type template in the outer region. The improvement observed in outer region errors when an M-star template is used supports the conclusion that the outer stars are predominantly dM-type, dK-type and other unclassified foreground stars of the Milky Way, (Sibbons et al. 2015).

[8] This supercedes the preliminary data stated in Sibbons et al. (2015) and is the result of more detailed work.

4.2 Rotation of the carbon star population

In the inner region, the $V_{\rm helio}$ of each C-type object was compared to the sample mean, $\langle V_{\rm helio}\rangle$, which we take to be the mean motion of the galaxy. This provides a measure of the motion of each object in the rest frame of the galactic centre of NGC 6822. Fig. 6 plots the locations of the inner C-stars, colour coded by the value of its residual velocity, $V_{\rm helio}-\langle V_{\rm helio}\rangle$, using a colour range from red (for positive values) to blue (for negative values). The colour range is consistent with red and blue shift and indicates whether an object is receding or approaching in the rest frame of NGC 6822. In the lower panel for 31 August, it can be seen that receding objects dominate the south east sector and approaching objects the north west sector, suggesting rotation of the C-star population about an axis, oriented approximately NE-SW. In the upper panel, for the night of 30 August, the pattern is less obvious but still apparent.

To examine this further, an axis of rotation was hypothesised lying in the plane of the sky and passing through a pivot point at the centre of the galaxy. The axis was rotated through 360 steps of 1°, starting at a position angle (PA) of 0°. At each step, the mean of the residual velocities of the stars on either side of the axis was computed. The subsample of stars falling on one side of the line is termed the 'North Bin', and for an axis with $PA=90°$, this is defined naturally. The subsample falling on the other side of the line is termed the 'South Bin'. Membership of each bin changes as the axis of rotation sweeps around and the value of its mean velocity residual also changes. By plotting the mean velocity residuals over 360°, a clear rotational signature is observed, see Fig. 7. The purple curves plot the mean rotational velocity of the 'North Bin' and the blue curves plot the mean rotational velocity of the 'South Bin'. In both bins and on both nights the curves rise and fall in opposition as the putative axis is rotated, confirming our impression of a rotating population. Furthermore, the curves for the 30 August and 31 August both suggest a similar sense of speed and rotation, even though the curves for 30 August are noisier.

The green curve in each case shows the sum of the average 'North' and 'South' velocities, which is generally offset from zero as the number of stars in the 'North' and 'South' bins is not always equal at each step. Over the full 360°, the offset should average to zero if the centre of the stellar sample and the pivot point of the hypothesised axis of rotation (the galaxy centre) are coincident. In this case, the green curve appears to lie mainly above the zero line, which suggests that the pivot point adopted does not coincide perfectly with the rotational centre of the sample. Changing the co-ordinates of the galactic centre in our analysis to the centre of the sample eliminates the offset, but has no significant effect on the rotation characteristics.

Using a least squares method, a sinusoid of the form $\hat{y} = V_{\rm rot}\sin(\theta-\theta_0)+y_0$ was fitted to the measured residual velocities, y, for each bin, such that $(\hat{y}-y)^2$ is minimised. The peak amplitude gives the mean rotational velocity, $V_{\rm rot}$, θ

Table 2. Summary of Results for spectra with $hght \geq 0.2$ and $|V_{\rm helio}| < 200$ km s^{-1}.

Template Object Composite Template	No. of Objects [2]	$\langle V_{\rm helio}\rangle$ [km s^{-1}] [3]	$\langle V_{err}\rangle$ [km s^{-1}] [4]	$\sigma(V_{\rm helio})$ [km s^{-1}] [5]	SE [km s^{-1}] [6]	Median $V_{\rm helio}$ [km s^{-1}] [7]
30August2011						
Inner region (C-template)	128	−45	±42	45	±4	−43
Outer region (C-template)	107	−20	±63	81	±8	−19
Outer region (M-template)	100	−28	±54	60	±6	−22
31August2011						
Inner region (C-template)	129	−51	±32	29	±3	−51
Outer region (C-template)	124	−17	±60	66	±6	−9
Outer region (M-template)	133	−18	±49	58	±5	−19

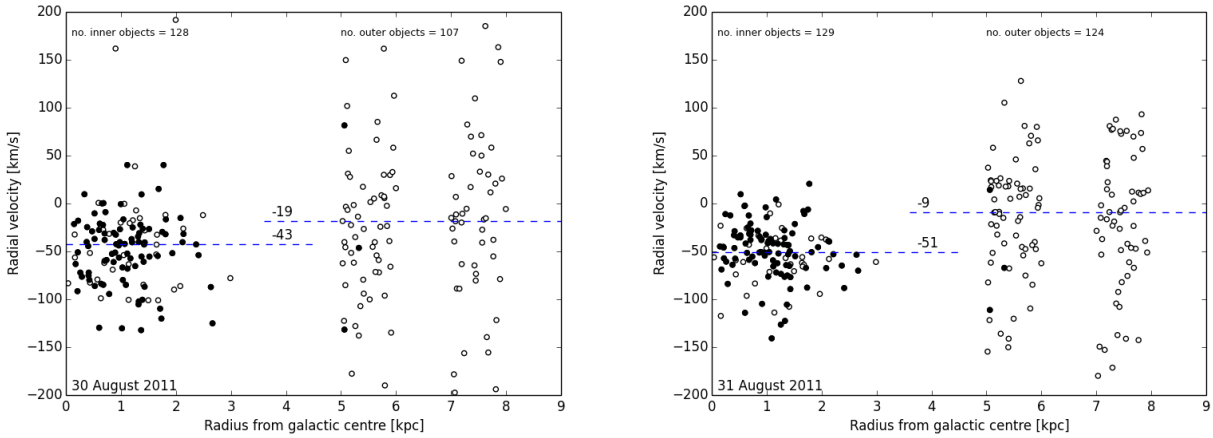

Figure 5. Relationship between $V_{\rm helio}$ and distance D from the galactic centre, left panel for 30 August 2011 and right panel for 31 August 2011. The horizontal dashed lines represent the median radial velocity of the sample from Table 2. C-type AGBs are shown as black points.

tracks the PA of the hypothesised axis and is stepped in 1° intervals, and θ_0 is the value of θ when $\hat{y} - y_0 = 0$. y_0 is the offset. Solving for y_0, θ_0 and $V_{\rm rot}$, $\hat{y}$ is plotted in Fig. 7, as dotted and dashed sinusoids for the 'North' and 'South' bins respectively. The rotation axis PA occurs at the peak of the sinusoid, so its PA is given by the value of θ when $\hat{y}$ is a maximum. This occurs at $\theta_0 \pm 90°$.

Table 3 provides a summary of the results obtained, with $V_{\rm rot}$ in column [1]. In column [2], we calculate the error in the velocity amplitude, $\Delta V_{\rm rot}$, from the RMS of the residual velocities found by deducting the sine function from each measured value over 360°, at the best fit PA. In columns [3] and [4], we show the PA of the galactic rotation axis and an estimate of its positional error found by taking the RMS, over 360°, of $\theta - \theta'$, where θ' is the angle which gives the value of $\hat{y}(\theta)$ in the sine function at the best fit PA. Column [5] shows the mean offset of the sinusoid due to the axis pivot point and the sample centre not being coincident.

The sense of rotation on both nights is the same and is such that the south eastern side is receding and the north western side is approaching, which corresponds with the rotation of HI gas in Weldrake et al. (2003). Moreover the rotation velocities and estimated PA for each night correspond within the estimated errors which gives us good confidence in the result. Nevertheless, owing to the better quality spectra for 31 August, better SNR and better error results, we take the results for 31 August, i.e $V_{\rm rot} = 11.4 \pm 2.1$ km s^{-1} and $PA = 26 \pm 13°$ as the more reliable.

Up to now, we have been considering only objects < 4 kpc from the galaxy centre . These correspond to objects in the Letarte et al. (2002) catalogue. Nevertheless there are 3 outliers at distances ~ 5 kpc, which lie close to the stellar ellipse in Fig. 2 and which are classified as C-type AGBs (Sibbons et al. 2015). These objects lie in positions close to the major axis of the ellipse. If we include these outliers in our estimates, the rotation rate and rotation axis become $V_{\rm rot} = 11.2 \pm 2.5$ km s^{-1} $PA = -5° \pm 20°$ for 30 August and $V_{\rm rot} = 12.1 \pm 2.3$ km s^{-1} $PA = 19° \pm 14°$ for 31 August, well within the margins of error for our sample.

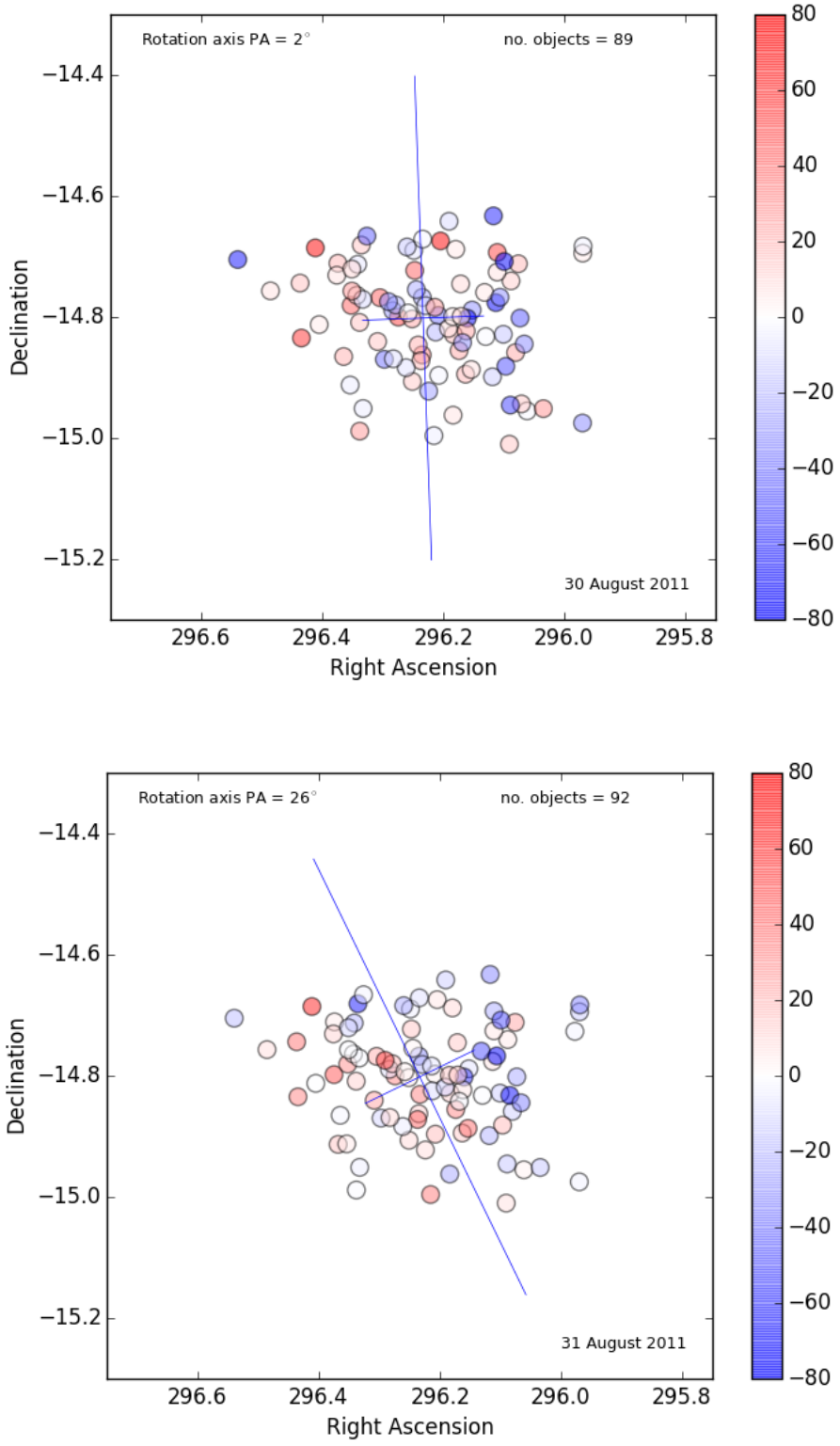

Figure 6. Residual velocity, $V_{\rm helio} - \langle V_{\rm helio} \rangle$, plots of the carbon star sample in the inner region of NGC6822. The long axis represents a derived axis of rotation and passes through the galaxy centre at the intersection with the short axis.

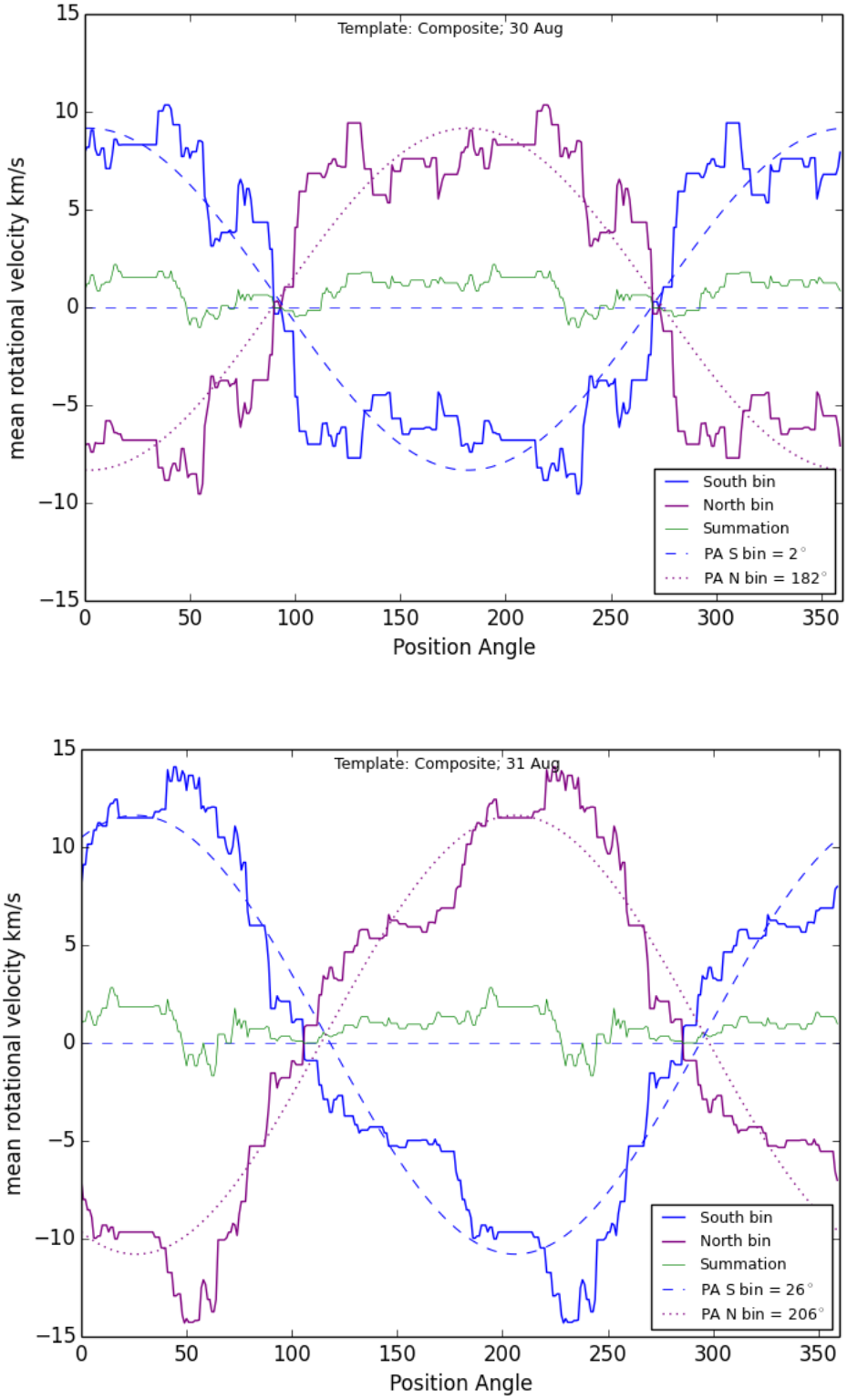

Figure 7. Rotational signature of carbon star component in NGC 6822 derived by plotting the mean residual velocities, $\langle V_{\rm helio} - \langle V_{\rm helio} \rangle \rangle$, on either side of the long axis as a function of its position angle.

Table 3. Summary of sinusoidal least squares fit to mean residual velocities.

	Rotation rate		Rotation axis		Offset
	$V_{\rm rot}$ km s^{-1} [1]	$\Delta V_{\rm rot}$ km s^{-1} [2]	PA ° [3]	ΔPA ° [4]	y_0 km s^{-1} [5]
30 Aug 2011	8.7	±2.2	2°	±22°	0.4
31 Aug 2011	11.2	±2.1	26°	±13°	0.4

Table 4. Comparison of results with published velocity data.

		$V_{\rm helio}$ km s^{-1}	$V_{\rm rot}$ km s^{-1}	Rotation axis PA	Comments
This study		-51 ± 3	11.2 ± 2.1	$26°\pm13°$	92 carbon stars
Koribalski et al. (2004)	[1]	-57 ± 2	...	...	HI measurements
Weldrake et al. (2003)	[2]	−53.3 to −54.7	−100 to +10	...	HI measurements
McConnachie (2012)		-57 ± 2.0	47 ± 2	...	$V_{\rm helio}$ from [1]
Mateo (1998)		...	47 ± 3	...	HI measurements
Mateo (1998)		-53 ± 4	...	...	Optical measurements
Kirby et al. (2014)		-54 ± 1.7	~ 10	...	7 red giant stars
Demers et al. (2006)	[3]	+10 to −70	...	63° to 67°	110 carbon stars
Veljanoski et al. (2015)		−59 to −60	12 ± 10	...	8 GCs, "disk" model, see §1
Flores-Durán et al. (2014)		−57.8	...	...	10 Planetary nebulae
Hwang et al. (2014)		-88.3 ± 22.7	....	...	4 Extended star clusters
Hwang et al. (2014)		-32.9 ± 29.4	15.9 ± 0.3	...	Derived from carbon star population of [3]

5 DISCUSSION AND CONCLUSION

Table 4 compares our results with the published data previously summarised in §1. The heliocentric radial velocity we obtained for NGC 6822 is -51 ± 3 km s^{-1}, based on the results from the better of the two nights of observations of a sample of its intermediate age carbon star population. This is a little lower than its HI counterpart - -57 ± 2 km s^{-1} - (Koribalski et al. 2004) but shows less than 1.6σ difference to this and the other estimates above, except that of Hwang et al. (2014) where it is apparent that the errors in Hwang et al. (2014) are large enough to include our result. In our sample, the grouping of objects in the inner and outer regions of the observed field indicates that the inner objects belong to NGC 6822, while the outer objects are more likely to be Milky Way stars, in support of the conclusion in Sibbons et al. (2015).

Rotation of the carbon star population about an axis having $PA = 26\pm13°$ has been shown with a rotation speed $V_{\rm rot} = 11.2\pm2.1$ km s^{-1}, based on the better of the two observing nights. While we see some movement in the PA of the rotation axis due to the AGB outliers in Fig. 2, their numbers are too small to draw any real conclusions on its significance. Radial velocity data from more objects spread broadly throughout the stellar ellipse in Fig. 2 would provide better data. Nevertheless, the sense of rotation of the sample is that the SE corner is receding and the NW corner is approaching, similar to the rotation of the HI disk (Weldrake et al. 2003). We can infer from Weldrake et al. (2003), that the PA of the rotation axis of the HI disk is $\sim 20°$ to $\sim 40°$ in the plane of the sky, assuming the rotation axis is perpendicular to the major axis of the gas disk. This is comparable to our estimate of the sky projected rotation axis of the C-type stellar population in this study. Thus we find that both axes are approximately coincident and the sense of rotation of the stars and gas is the same, leading us to conclude that NGC 6822 is not a PRG.

The PA of the major axes of the isodensity contours of the RGB stars in Demers et al. (2006) varies from 80° for the innermost contour (radius= 10′) to 65° for the outermost contour (radius= 35′). Our inner sample has a angular radius of $\sim 17'$, and so falls between these extremes. Hence, there is a misalignment of $\sim 45°$ between our rotation axis and the respective isodensity profile. Furthermore, since $V_{\rm rot}$ is derived from mean velocities, it is reasonable to adopt the mean distance of our carbon star sample from the galaxy centre as a basis for further comparative discussion. This distance is $\langle D \rangle = 1.1$ kpc. Interpreting the velocity diagrams of Weldrake et al. (2003), the rotation speed of the HI disk can be estimated to be ~ 30 km s^{-1} at 1.1 kpc (≈ 8 arcmin) from the galactic centre. This rotation speed is faster than our C-star sample confirming differences in the rotation speeds of the rotationally supported gas and the pressure supported intermediate age stellar populations.

The rotation misalignment, apparent separation of gas and stellar populations and effect of AGBs filling the gap between the central sample in this study and the stellar ellipse depicted in Fig. 2 would benefit from further study, particularly at higher SNR and better resolving power.

ACKNOWLEDGEMENTS

We would like to thank Scott Croom for undertaking the AAOmega service observations and Sarah Brough for her assistance in reducing the data.

We would also like to thank the anonymous referee for useful comments, which has helped us to write a more concise paper.

REFERENCES

Battinelli P., Demers S., Kunkel W. E., 2006, A&A, 451, 99
Demers S., Battinelli P., 2007, in Kerschbaum F., Charbonnel C., Wing R. F., eds, Astronomical Society of the Pacific Conference Series Vol. 378, Why Galaxies Care About AGB Stars: Their Importance as Actors and Probes. p. 469
Demers S., Battinelli P., Kunkel W. E., 2006, ApJ, 636, L85
Feast M. W., Whitelock P. A., Menzies J. W., Matsunaga N., 2012, MNRAS, 421, 2998
Flores-Durán S. N., Peña M., Hernández-Martínez L., García-Rojas J., Ruiz M. T., 2014, A&A, 568, A82
Gieren W., Pietrzyński G., Nalewajko K., Soszyński I., Bresolin F., Kudritzki R.-P., Minniti D., Romanowsky A., 2006, ApJ, 647, 1056
Hodge P., Smith T., Eskridge P., MacGillivray H., Beard S., 1991, ApJ, 379, 621
Hubble E., 1925, Contributions from the Mount Wilson Observatory / Carnegie Institution of Washington, 304, 1
Hwang N., Park H. S., Lee M. G., Lim S., Hodge P. W., Kim S. C., Miller B., Weisz D., 2014, ApJ, 783, 49
Kirby E. N., Bullock J. S., Boylan-Kolchin M., Kaplinghat M., Cohen J. G., 2014, MNRAS, 439, 1015
Koribalski B. S., et al., 2004, AJ, 128, 16
Letarte B., Demers S., Battinelli P., Kunkel W. E., 2002, AJ, 123, 832
Mateo M. L., 1998, ARA&A, 36, 435
Matthews L. D., Gérard E., Le Bertre T., 2015, MNRAS, 449, 220
McConnachie A. W., 2012, AJ, 144, 4
Rich J. A., Persson S. E., Freedman W. L., Madore B. F., Monson A. J., Scowcroft V., Seibert M., 2014, ApJ, 794, 107
Sibbons L. F., Ryan S. G., Cioni M.-R. L., Irwin M., Napiwotzki R., 2012, A&A, 540, A135
Sibbons L. F., Ryan S. G., Napiwotzki R., Thompson G. P., 2015, A&A, 574, A102
Tonry J., Davis M., 1979, AJ, 84, 1511
Veljanoski J., et al., 2015, MNRAS, 452, 320
Weldrake D. T. F., de Blok W. J. G., Walter F., 2003, MNRAS, 340, 12
Whitelock P. A., Menzies J. W., Feast M. W., Nsengiyumva F., Matsunaga N., 2013, MNRAS, 428, 2216
de Blok W. J. G., Walter F., 2000, ApJ, 537, L95
van Belle G. T., Paladini C., Aringer B., Hron J., Ciardi D., 2013, ApJ, 775, 45

APPENDIX A: TABLES OF DATA

Appendix A1 shows the individual *fxcor* returns for objects meeting the criteria *hght*$\geqslant 0.2$, -200 km s^{-1} $\leqslant V_{\rm helio} \leqslant +200$ km s^{-1} for 30 August 2011 and 31 August 2011. The meanings of the data in each column are described as follows:

Column	
1 & 2	Fibre number and the target identifier respectively as defined by Sibbons et al. (2015).
3 & 4	Right ascension (RA) and declination (Dec) of each object (J2000) according to Sibbons et al. (2015).
5	$I-$band magnitude of C-type AGBs in the inner region from the catalogue of Letarte et al. (2002).
6	Distance of the object from the putative galactic centre ($\alpha = 19^h:44^m:56^s$ (296.2333°), J2000 and $\delta = -14°:48':06''$ ($-14.8017°$), J2000) centred on the optical co-ordinates of NGC 6822[9] adopted by Sibbons et al. (2012, 2015) and a galactic distance of 490 kpc (Mateo 1998).
7 & 8	Photometric classification of each object from Sibbons et al. (2012), and its corresponding spectroscopic classification from Sibbons et al. (2015).
9 & 13	*SNR* of each object calculated in the band 8560 Å to 8650 Å for the nights of 30 August 2011 and 31 August 2011 respectively.
10, 11 & 12	*hght*, the heliocentric radial velocity ($V_{\rm helio}$) and the velocity error ($V_{\rm err}$) returned from *fxcor* for the night of 30 August 2011.
14, 15 & 16	*hght*, the heliocentric radial velocity ($V_{\rm helio}$) and the velocity error ($V_{\rm err}$) returned from *fxcor* for the night of 31 August 2011.
17	Flag showing which objects were used in the composite templates: "C" for the C-type composite and "M" for the M-type composite.

Appendix A1: Individual *fxcor* returns for objects meeting the criteria ($hght \geqslant 0.2$, -200 km s$^{-1} \leqslant V_{\rm helio} \leqslant +200$ km s^{-1}).

[1]	[2]	[3]	[4]	[5]	[6]	[7]	[8]	[9]	[10]	[11]	[12]	[13]	[14]	[15]	[16]	[17]
								30 August 2011				31 August 2011				
#Fibre	ID	RA (°)	Dec (°)	$I-$band (mag.)	distance (kpc)	phot. class.	spec. class.	*SNR*	*hght*	$V_{\rm helio}$ (km s^{-1})	$V_{\rm err}$ (km s^{-1})	*SNR*	*hght*	$V_{\rm helio}$ (km s^{-1})	$V_{\rm err}$ (km s^{-1})	Flag
1	217716	296.23	-14.86	19.3	0.52	M	Ce:	7	0.39	-10	49	9	0.48	-35	36	C
2	239630	296.33	-14.95	19.4	1.52	C*	C:	6	0.43	-55	41	7	0.54	-55	27	C
3	210316	296.43	-14.83	18.9	1.69	M	C:	5	0.59	15	25	6	0.76	-11	16	C
4	174035	296.37	-14.71	19.1	1.4	M*	C	3	0.37	-26	57	5	0.27	-43	67	C
6	199974	296.37	-14.8	19.2	1.17	M	C	...	...	...	...	9	0.65	4	24	C
7	194949	296.35	-14.78	18.9	1	C*	C:	12	0.72	-1	34	18	0.75	-14	23	C
8	242030	296.35	-14.96	18.8	1.64	...	...	6	0.6	-53	21	9	0.7	-62	22	...
9	220271	296.39	-14.87	...	1.43	...	...	5	0.48	-28	40	8	0.59	-63	27	...
10	188246	296.49	-14.76	18.3	2.12	M	C:	6	0.57	-40	29	10	0.8	-39	16	C
11	172656	296.54	-14.71	19.3	2.66	C*	C	5	0.29	-125	69	8	0.39	-70	41	C
12	211898	296.31	-14.84	18.8	0.7	M	C	9	0.57	-31	26	7	0.74	-21	20	C
14	246838	296.54	-14.98	...	2.99	...	...	4	0.36	-78	37	5	0.57	-61	28	...
15	206867	296.3	-14.82	...	0.59	...	...	7	0.42	1	58	8	0.42	-3	38	...
17	225812	296.32	-14.9	...	1.06	...	...	4	0.33	0	75	6	0.51	-10	31	...
18	190283	296.34	-14.76	19.6	0.96	M	C	6	0.45	-44	33	5	0.36	-51	36	C
19	168284	296.41	-14.69	19.0	1.78	C*	C:	9	0.48	40	42	10	0.48	21	34	C
21	213379	296.24	-14.85	19.9	0.39	C*	Ce:	4	0.4	-25	42	...	...	...	...	C
22	200573	296.27	-14.8	19.0	0.34	M	Ce	8	0.37	10	73	9	0.72	-12	17	C
23	219598	296.3	-14.87	19.0	0.79	C*	C	6	0.36	-94	77	10	0.48	-62	52	C
24	203106	296.34	-14.81	19.4	0.87	C*	C:	7	0.64	-31	30	9	0.68	-35	21	C
25	209216	296.23	-14.83	19.1	0.25	M	Ce	...	...	...	...	12	0.64	-11	21	C
26	197590	296.32	-14.79	19.3	0.72	C*	M:	22	0.68	-9	43	9	0.45	-28	63	...
28	197464	296.28	-14.79	19.0	0.43	M	C	7	0.48	-80	47	9	0.7	-58	30	C
29	206129	296.24	-14.82	19.2	0.16	M	dKe:	12	0.6	-32	39	12	0.54	-23	49	...
31	180514	296.38	-14.73	17.8	1.33	M	C	10	0.83	-40	15	11	0.89	-36	16	C
32	191382	296.3	-14.77	19.2	0.66	M*	C	6	0.5	0	28	8	0.51	-25	22	C
33	306281	297.06	-15.27	...	7.9	...	...	4	0.26	148	63	...	...	...	...	...
34	294767	296.99	-15.21	...	7.19	...	...	5	0.23	149	92	...	...	...	...	...
36	292760	296.77	-15.2	...	5.6	M	dM	23	0.57	5	50	48	0.61	7	51	M
38	218420	296.36	-14.87	19.0	1.21	C*	C	7	0.43	-25	26	7	0.32	-52	73	C
41	324220	297.01	-15.36	...	8	...	...	1	0.21	-6	26	...	...	...	...	...
43	229856	296.37	-14.91	19.0	1.47	C*	C	...	...	...	...	8	0.52	-31	31	C
45	201454	296.25	-14.8	19.4	0.15	C*	Ce:	16	0.58	-21	45	21	0.66	-45	36	C
47	291854	296.82	-15.2	...	5.92	...	...	...	...	...	...	5	0.3	80	51	...
48	184448	296.44	-14.74	19.0	1.75	M*	C	4	0.3	-30	48	7	0.31	-6	38	C
49	335226	296.92	-15.41	...	7.68	...	...	5	0.31	-156	63	7	0.26	2	69	...
51	341622	296.86	-15.44	...	7.55	...	...	4	0.23	71	106	...	...	...	...	...
52	342923	296.85	-15.45	...	7.52	...	...	2	0.28	33	60	...	...	...	...	...
53	248633	296.34	-14.99	18.9	1.82	C*	C:	6	0.46	-17	46	7	0.47	-51	38	C
54	229643	296.35	-14.91	18.9	1.37	C*	C	8	0.64	-55	24	10	0.71	-43	23	C
56	351371	296.84	-15.49	...	7.73	...	...	3	0.28	58	138	...	...	...	...	...
57	186954	296.47	-14.75	21.0	2	Unid*	dK	4	0.24	192	76	4	0.22	-35	65	...
58	249091	296.39	-14.99	...	2.08	...	...	7	0.47	-86	20	7	0.44	-38	46	...
62	299244	296.68	-15.24	...	5.22	...	...	...	...	...	...	4	0.28	19	62	...
65	220153	296.24	-14.87	19.6	0.6	M	Ce	9	0.31	-28	101	8	0.59	-2	31	C
68	240673	296.06	-14.96	19.7	1.93	M*	C	3	0.31	-52	66	4	0.36	-46	64	C
69	310311	296.6	-15.29	...	5.2	...	...	4	0.37	-178	72	6	0.33	-32	68	...
70	237395	296.07	-14.94	19.9	1.81	Unid*	C	3	0.26	-32	133	...	...	...	...	C
71	228306	296.25	-14.91	19.8	0.91	M	Ce	5	0.39	-33	61	6	0.56	-38	29	C
73	337540	296.5	-15.42	...	5.74	...	...	3	0.3	9	84	...	...	...	...	...
75	223056	296.26	-14.88	19.6	0.74	M	Ce	6	0.42	-59	55	9	0.33	-55	52	C
76	237999	296.09	-14.95	20.0	1.71	C*	C	4	0.24	-110	37	5	0.48	-67	27	C
78	220391	296.21	-14.87	...	0.63	...	...	9	0.64	-24	33	11	0.66	-26	30	...

Continued on next page

Appendix A1 (cont.): Individual *fxcor* returns for objects meeting the criteria ($hght \geqslant 0.2$, -200 km s^{-1} $\leqslant V_{\rm helio} \leqslant +200$ km s^{-1}).

[1]	[2]	[3]	[4]	[5]	[6]	[7]	[8]	[9]	[10]	[11]	[12]	[13]	[14]	[15]	[16]	[17]
								30 August 2011				31 August 2011				
#Fibre	ID	RA (°)	Dec (°)	$I-$band (mag.)	distance (kpc)	phot. class.	spec. class.	*SNR*	*hght*	$V_{\rm helio}$ (km s^{-1})	$V_{\rm err}$ (km s^{-1})	*SNR*	*hght*	$V_{\rm helio}$ (km s^{-1})	$V_{\rm err}$ (km s^{-1})	Flag
80	231793	296.22	-14.92	19.0	1.04	C*	C	4	0.5	-80	57	9	0.79	-39	21	C
81	219171	296.23	-14.87	...	0.57	...	...	7	0.46	-79	36	8	0.72	-61	17	...
82	343626	296.38	-15.45	...	5.69	...	...	4	0.49	-72	24	...	...	...	...	...
83	343571	296.44	-15.45	...	5.81	...	...	...	...	...	...	6	0.42	71	56	...
84	248651	296.28	-14.99	18.9	1.65	...	...	7	0.63	-43	29	10	0.85	-56	14	...
85	208620	296.1	-14.83	18.5	1.12	M	C	11	0.8	-68	23	11	0.85	-66	17	C
86	219351	296.28	-14.87	19.4	0.7	M	Ce	7	0.52	-60	47	9	0.76	-38	22	C
88	226097	296.21	-14.9	19.3	0.84	M	C	5	0.53	-53	27	5	0.65	-29	21	C
90	215861	296.17	-14.86	19.5	0.67	M	Ce	5	0.5	-22	37	6	0.5	-13	26	C
91	250173	296.22	-15	19.2	1.67	Unid*	C	6	0.39	-55	58	4	0.44	-8	29	C
94	225648	296.16	-14.89	18.8	0.98	C*	C	11	0.84	-27	14	9	0.86	-33	16	C
95	242563	296.18	-14.96	19.8	1.43	C*	C	7	0.41	-41	58	9	0.64	-77	25	C
96	208714	296.18	-14.83	19.3	0.48	M	Ce	8	0.64	-29	22	11	0.74	-35	17	C
98	226603	296.12	-14.9	18.7	1.26	M	C	6	0.65	-65	24	7	0.71	-74	23	C
99	330842	296.34	-15.39	...	5.08	M	dM	3	0.32	-46	62	7	0.32	24	62	M
101	220672	296.11	-14.87	...	1.22	...	...	3	0.36	-18	41	5	0.49	-1	35	...
102	344297	296.12	-15.46	...	5.66	M	dM	5	0.35	85	56	12	0.52	16	46	M
104	209650	296.13	-14.83	19.4	0.9	M	C	6	0.37	-51	33	7	0.35	-51	39	C
105	233186	296.16	-14.93	20.2	1.26	Unid*	Unid	19	0.52	39	42	17	0.71	-39	26	...
106	344467	296.18	-15.46	...	5.61	M	dK	7	0.48	-40	33	15	0.61	-14	44	...
107	351774	296.12	-15.49	...	6	...	...	3	0.29	16	55	6	0.53	-62	30	...
112	253239	296.09	-15.01	19.4	2.14	C*	C	3	0.35	-32	26	4	0.49	-40	24	C
113	199754	296.21	-14.8	19.2	0.21	C*	Ce	10	0.5	-92	54	8	0.67	-45	21	C
115	339686	296.09	-15.43	...	5.52	...	...	4	0.31	-100	52	...	...	...	...	...
116	326339	295.95	-15.37	...	5.41	...	...	4	0.29	-94	75	4	0.46	24	48	...
119	207586	296.21	-14.82	19.1	0.26	M	C	11	0.6	-72	35	8	0.6	-61	32	C
122	223739	296.15	-14.89	19.8	0.98	M	C	5	0.5	-40	36	7	0.44	-4	71	C
123	199930	296.24	-14.8	...	0.04	...	...	14	0.78	-83	26	14	0.78	-56	23	...
124	239687	296.03	-14.95	19.3	2.08	M*	C	7	0.4	-15	54	5	0.65	-67	20	C
125	216688	296.08	-14.86	18.8	1.36	M*	C:	16	0.74	-22	18	14	0.75	-64	21	C
126	327377	296.01	-15.37	...	5.23	M	dK	6	0.43	-2	45	8	0.31	-9	86	...
128	317678	295.95	-15.33	...	5.09	M	dM:	5	0.23	-3	60	9	0.35	17	72	M
129	337831	295.92	-15.42	...	5.89	M	dK	4	0.37	30	36	7	0.39	36	66	...
130	313097	295.88	-15.31	...	5.23	M	dK	6	0.34	-62	114	12	0.48	-11	57	...
131	355390	295.77	-15.51	...	7.18	M	dM:	...	...	...	...	11	0.38	45	185	M
132	300999	295.84	-15.25	...	5.02	...	...	...	...	...	...	5	0.23	-155	63	...
133	372253	295.8	-15.59	...	7.68	M	dK	7	0.35	30	115	8	0.41	70	68	...
134	317557	295.79	-15.33	...	5.79	M	dK:	5	0.49	6	52	7	0.41	16	80	...
135	303607	295.81	-15.26	...	5.25	M	dM	...	...	...	...	7	0.39	26	94	M
136	222468	296.1	-14.88	19.5	1.32	M	C	4	0.47	-105	31	7	0.59	-28	39	C
137	299996	295.78	-15.24	...	5.32	M	C:	3	0.42	-46	32	5	0.53	-67	38	...
138	297583	295.8	-15.23	...	5.12	M	dM	8	0.44	-7	59	16	0.57	58	57	M
139	303122	295.74	-15.26	...	5.62	M	dM	...	...	...	...	7	0.59	15	41	M
141	310841	295.78	-15.3	...	5.67	...	...	...	...	...	...	8	0.46	-54	51	...
142	309370	295.87	-15.29	...	5.13	M	dM	8	0.37	31	63	...	...	...	...	M
145	350411	295.59	-15.49	...	7.93	M	dK	5	0.24	26	103	8	0.48	-51	53	...
147	340026	295.62	-15.43	...	7.4	...	...	4	0.23	52	77	4	0.26	-92	169	...
148	276398	295.72	-15.13	...	5.06	C	C:	5	0.36	-132	46	9	0.65	-111	26	...
149	332677	295.65	-15.4	...	7	M	dM:	5	0.35	-15	28	10	0.42	-29	50	M
152	336076	295.52	-15.41	...	7.89	...	...	3	0.3	-79	36	5	0.46	-39	56	...
153	337060	295.6	-15.42	...	7.45	...	...	3	0.26	-73	76	7	0.39	73	86	...
154	282194	295.69	-15.16	...	5.41	...	...	2	0.41	-27	72	4	0.39	-68	28	...
155	332908	295.52	-15.4	...	7.77	...	...	4	0.44	-38	31	5	0.38	11	76	...
156	329347	295.52	-15.38	...	7.72	M	dM:	7	0.36	12	53	12	0.55	-47	47	M
157	324005	295.54	-15.36	...	7.46	M	dM:	...	...	...	...	9	0.47	-82	46	M

Continued on next page

Appendix A1 (cont.): Individual *fxcor* returns for objects meeting the criteria ($hght \geqslant 0.2$, -200 km s^{-1} $\leqslant V_{\rm helio} \leqslant +200$ km s^{-1}).

[1]	[2]	[3]	[4]	[5]	[6]	[7]	[8]	[9]	[10]	[11]	[12]	[13]	[14]	[15]	[16]	[17]
								30 August 2011				31 August 2011				
#Fibre	ID	RA (°)	Dec (°)	$I-$band (mag.)	distance (kpc)	phot. class.	spec. class.	*SNR*	*hght*	$V_{\rm helio}$ (km s^{-1})	$V_{\rm err}$ (km s^{-1})	*SNR*	*hght*	$V_{\rm helio}$ (km s^{-1})	$V_{\rm err}$ (km s^{-1})	Flag
158	312062	295.53	-15.3	...	7.19	M	dM:	8	0.4	-20	51	15	0.53	-16	60	M
159	318572	295.58	-15.33	...	7.08	M	dK	10	0.54	-19	52	15	0.61	-15	33	...
160	312215	295.5	-15.3	...	7.43	M	dK	...	...	...	...	10	0.31	-9	94	...
161	301044	295.48	-15.25	...	7.29	...	...	...	...	...	...	1	0.31	-171	36	...
163	298121	295.48	-15.23	...	7.24	M	dM:	...	...	...	...	8	0.38	81	68	M
164	305736	295.49	-15.27	...	7.32	M	dK	...	...	...	...	11	0.34	-19	89	...
165	271722	295.63	-15.1	...	5.63	...	...	4	0.37	-71	43	7	0.35	128	66	...
166	301701	295.43	-15.25	...	7.68	...	...	...	...	...	...	4	0.24	-67	77	...
167	277183	295.64	-15.13	...	5.65	M	dM	10	0.25	66	100	...	...	...	...	M
169	287590	295.45	-15.18	...	7.24	...	...	3	0.28	-156	42	6	0.49	-9	59	...
171	276077	295.43	-15.12	...	7.19	...	...	5	0.31	-63	36	8	0.29	15	62	...
172	289833	295.41	-15.19	...	7.6	M	dK	10	0.43	-17	71	15	0.73	-61	39	...
173	286135	295.42	-15.17	...	7.45	M	dM	7	0.33	-80	52	10	0.35	-49	60	M
174	245610	295.97	-14.98	19.2	2.63	M	C	3	0.33	-87	54	4	0.72	-53	28	C
176	248935	295.55	-14.99	...	5.91	...	...	2	0.24	-135	100	...	...	...	...	...
178	246831	295.64	-14.98	...	5.14	M	dK:	5	0.48	55	37	9	0.53	-9	52	...
180	267519	295.6	-15.08	...	5.78	...	...	2	0.3	162	69	...	...	...	...	...
181	254251	295.4	-15.02	...	7.09	M	dK	12	0.55	7	38	19	0.69	-2	46	...
183	222762	295.59	-14.88	...	5.33	M	dM	...	...	...	...	9	0.29	105	59	M
184	223794	295.55	-14.89	...	5.72	M	dM	10	0.31	-24	79	12	0.35	9	51	M
185	215764	295.52	-14.86	...	5.88	M	dMe:	5	0.31	-39	81	8	0.3	-40	54	M
186	223551	295.62	-14.89	...	5.11	M	dK	5	0.3	102	100	9	0.45	-52	56	...
187	202875	296.09	-14.81	...	1.16	...	...	4	0.4	-21	47	8	0.61	-36	37	...
188	239242	295.56	-14.95	...	5.71	...	...	...	...	...	...	6	0.39	-75	42	...
189	234263	295.54	-14.93	...	5.84	M	dM:	6	0.39	-24	32	12	0.37	-85	31	M
190	220386	295.54	-14.87	...	5.8	M	dK	7	0.38	-190	49	9	0.54	-110	43	...
191	183391	296.09	-14.74	18.5	1.31	C*	C	6	0.41	-34	41	5	0.52	-43	48	C
193	193714	296.11	-14.78	19.4	1.02	C*	C	7	0.42	-130	59	9	0.72	-41	26	C
194	184165	295.61	-14.74	...	5.18	M	dM:	5	0.41	-22	53	7	0.44	24	81	M
195	208174	295.51	-14.83	...	5.96	M	dMe	5	0.44	113	76	9	0.55	5	70	M
198	178893	296.11	-14.73	19.0	1.2	C*	C	6	0.55	-40	49	6	0.69	-42	24	C
199	185402	295.52	-14.75	...	5.95	M	dMe	16	0.49	58	47	20	0.66	-2	49	M
201	197170	296.15	-14.79	19.0	0.68	M	Ce	7	0.72	-85	20	6	0.73	-59	22	C
202	201578	295.53	-14.8	...	5.83	M	dMe:	9	0.45	-2	54	15	0.47	-43	34	M
203	216118	296.07	-14.86	...	1.41	...	...	5	0.46	-85	29	6	0.47	-108	41	...
204	209652	296.08	-14.83	19.3	1.26	C*	C:	...	...	...	...	6	0.44	-126	48	C
205	201803	295.62	-14.8	...	5.06	M	dM:	4	0.46	-122	50	5	0.3	-122	53	M
206	188974	296.13	-14.76	19.2	0.92	M	Ce	7	0.48	-42	33	8	0.66	-105	19	C
207	201131	296.16	-14.8	19.2	0.61	M	C	8	0.64	-130	25	9	0.72	-114	28	C
208	191195	296.11	-14.77	19.5	1.09	M	C	5	0.46	-85	27	6	0.44	-141	45	C
209	200928	295.56	-14.8	...	5.58	M	dMe:	6	0.32	-45	69	9	0.52	-18	42	M
210	201043	296.07	-14.8	19.1	1.33	M	C	4	0.38	-102	44	5	0.58	-77	21	C
211	205865	296.19	-14.82	19.3	0.38	C*	Ce	8	0.55	-40	41	12	0.8	-64	23	C
213	143954	295.41	-14.57	...	7.11	M	dM	3	0.34	-89	39	5	0.36	-37	50	M
214	212970	296.07	-14.84	19.5	1.43	M*	C	5	0.3	-87	88	7	0.31	-89	56	C
216	217770	296	-14.86	...	1.97	...	...	4	0.26	-90	44	4	0.46	-94	38	...
218	135229	295.57	-14.53	...	5.94	...	...	...	...	...	...	2	0.21	66	65	...
219	203778	296.03	-14.81	...	1.68	...	...	4	0.29	-101	94	3	0.48	-64	53	...
220	207096	296.16	-14.82	19.3	0.62	M	C	5	0.61	-21	25	5	0.4	-42	60	C
221	170279	295.97	-14.69	19.0	2.37	M	C	4	0.66	-43	24	7	0.76	-65	18	C
222	147856	295.59	-14.59	...	5.65	...	...	4	0.31	-54	66	4	0.45	-45	60	...
223	235703	296.02	-14.94	...	2.13	...	...	2	0.46	-26	61	4	0.44	-58	58	...
225	166319	296.11	-14.68	...	1.5	...	...	3	0.36	-101	31	5	0.46	-71	49	...
226	170004	296.11	-14.69	19.6	1.37	Unid*	C	5	0.34	10	77	3	0.41	-75	39	C
228	212351	296.17	-14.84	19.7	0.64	M	C	5	0.53	-84	42	6	0.69	-52	18	C

Continued on next page

Appendix A1 (cont.): Individual *fxcor* returns for objects meeting the criteria ($hght \geqslant 0.2$, -200 km s^{-1} $\leqslant V_{\rm helio} \leqslant +200$ km s^{-1}).

[1]	[2]	[3]	[4]	[5]	[6]	[7]	[8]	[9]	[10]	[11]	[12]	[13]	[14]	[15]	[16]	[17]
								30 August 2011				31 August 2011				
#Fibre	ID	RA (°)	Dec (°)	$I-$band (mag.)	distance (kpc)	phot. class.	spec. class.	*SNR*	*hght*	$V_{\rm helio}$ (km s^{-1})	$V_{\rm err}$ (km s^{-1})	*SNR*	*hght*	$V_{\rm helio}$ (km s^{-1})	$V_{\rm err}$ (km s^{-1})	Flag
229	167638	295.97	-14.68	18.7	2.41	M*	C	6	0.5	-54	34	7	0.83	-88	16	C
230	174226	296.08	-14.71	19.5	1.51	M	C	2	0.43	-27	63	3	0.44	-21	33	C
232	100740	295.42	-14.34	...	7.82	...	...	3	0.2	-122	173	5	0.27	93	86	...
233	179746	296.22	-14.73	...	0.64	...	...	6	0.45	-99	31	6	0.54	-96	32	...
235	173378	296.1	-14.71	19.2	1.37	C*	C	5	0.46	-132	28	4	0.55	-106	40	C
236	92831	295.56	-14.3	...	7.03	...	...	...	...	...	...	8	0.22	-180	54	...
237	88989	295.46	-14.28	...	7.77	M	dM	6	0.22	-55	80	10	0.42	-143	56	M
238	186430	296.23	-14.75	19.0	0.44	M	Unid	13	0.46	-83	59	9	0.56	-74	31	...
242	78560	295.53	-14.23	...	7.63	M	dK	7	0.33	-15	76	13	0.55	-46	51	...
244	67411	295.58	-14.17	...	7.62	...	...	2	0.26	185	88	...	...	...	...	...
245	86214	295.59	-14.27	...	7.01	M	dM	10	0.38	29	49	...	...	...	...	M
246	191318	296.23	-14.77	18.9	0.29	C*	C	14	0.68	-76	21	10	0.79	-84	21	C
252	195133	296.23	-14.78	19.4	0.18	C*	Ce:	12	0.53	-63	42	10	0.6	-69	27	C
254	64581	295.6	-14.16	...	7.57	M	dM:	5	0.56	-41	31	9	0.55	-42	42	M
255	93873	295.87	-14.31	...	5.19	...	...	2	0.28	-52	67	3	0.25	-23	51	...
256	50172	295.62	-14.09	...	7.94	...	...	...	...	...	...	2	0.35	14	64	...
257	184858	296.17	-14.75	19.6	0.7	M	C	5	0.4	-38	49	7	0.6	-33	28	C
258	173834	296.22	-14.71	...	0.79	...	...	6	0.44	-32	50	7	0.69	-83	23	...
259	49090	295.74	-14.09	...	7.39	...	...	...	...	...	...	6	0.36	-137	119	...
260	195884	296.21	-14.78	19.5	0.22	M	C	9	0.62	-18	24	11	0.73	-57	21	C
261	83041	295.91	-14.25	...	5.4	...	...	4	0.38	-80	65	4	0.39	-141	59	...
262	165760	296.2	-14.67	20.1	1.12	M	C	6	0.44	40	37	6	0.49	-42	51	C
263	107892	295.81	-14.38	...	5.03	M	dK	5	0.38	-62	82	10	0.33	-82	88	...
266	200300	296.18	-14.8	19.7	0.41	M	Ce:	8	0.44	-44	50	8	0.53	-33	27	C
267	158986	296.19	-14.64	19.2	1.41	M	C	5	0.61	-61	36	5	0.5	-65	45	C
268	157078	296.12	-14.63	18.2	1.74	M	C:	6	0.66	-120	36	8	0.8	-88	22	C
269	200182	296.17	-14.8	18.9	0.52	C*	Ce	7	0.69	-37	27	9	0.67	-33	37	C
271	42925	295.84	-14.06	...	7.15	...	...	3	0.37	-89	67	7	0.3	-153	75	...
273	172060	296.2	-14.7	19.6	0.9	C*	dK	4	0.36	162	98	6	0.23	-38	96	...
274	168826	296.18	-14.69	19.0	1.07	M	C	5	0.67	-42	34	9	0.69	-37	29	C
277	76159	295.96	-14.22	...	5.5	...	...	...	...	...	...	8	0.26	-120	69	...
279	181364	296.13	-14.73	...	1.05	...	...	9	0.69	-54	26	9	0.64	-71	28	...
281	30076	295.97	-13.99	...	7.3	...	...	4	0.33	82	56	7	0.49	-23	34	...
282	22972	295.99	-13.95	...	7.55	...	...	4	0.42	50	36	6	0.49	76	35	...
283	194386	296.19	-14.78	...	0.44	...	...	10	0.76	-52	21	10	0.86	-59	15	...
284	173114	296.33	-14.71	18.6	1.14	M*	dM:	19	0.82	-63	22	...	...	...	...	...
285	78272	296.07	-14.23	...	5.09	M	dM:	...	...	...	...	7	0.48	23	47	M
286	27278	296.08	-13.97	...	7.19	M	dM:	...	...	...	...	9	0.39	44	89	M
287	179183	295.98	-14.73	19.7	2.21	C*	C	...	...	...	...	4	0.44	-53	32	C
289	64658	296.14	-14.16	...	5.53	...	...	4	0.42	1	47	5	0.42	46	60	...
290	192177	296.33	-14.77	19.7	0.87	M	C	4	0.43	-61	56	5	0.59	-51	20	C
291	74535	296.29	-14.21	...	5.08	...	...	3	0.26	-85	46	6	0.27	-62	47	...
292	169202	296.25	-14.69	19.1	0.96	M	C	5	0.57	-56	46	7	0.66	-54	15	C
293	159727	296.25	-14.65	...	1.34	...	...	3	0.5	-15	28	5	0.47	-57	33	...
294	17384	296.22	-13.92	...	7.51	...	...	...	...	...	...	5	0.38	-5	42	...
295	165127	296.23	-14.67	18.8	1.12	M	C	6	0.76	-52	19	8	0.68	-59	20	C
296	171315	296.4	-14.7	...	1.66	...	...	5	0.5	-33	37	5	0.69	-66	14	...
297	21034	296.25	-13.94	...	7.36	M	dK	4	0.45	70	43	7	0.65	-104	36	...
298	194777	296.28	-14.78	19.0	0.42	C*	Ce:	9	0.61	-72	37	9	0.72	-29	23	C
301	164620	296.22	-14.67	...	1.14	...	...	4	0.62	-101	29	6	0.63	-114	32	...
302	182253	296.31	-14.74	...	0.85	...	...	5	0.58	-69	38	5	0.62	-33	25	...
304	62395	296.37	-14.15	...	5.68	M	dM	6	0.46	-59	52	...	...	...	...	M
305	167938	296.26	-14.68	18.8	1.03	M*	C	5	0.55	-67	41	7	0.82	-76	18	C
306	12243	296.36	-13.9	...	7.81	M	dM:	6	0.4	21	39	8	0.37	10	46	M
307	20479	296.33	-13.94	...	7.43	M	dK	8	0.4	-65	53	9	0.61	-26	43	...

Continued on next page

Appendix A1 (cont.): Individual *fxcor* returns for objects meeting the criteria ($hght \geqslant 0.2$, -200 km s^{-1} $\leqslant V_{\rm helio} \leqslant +200$ km s^{-1}).

[1]	[2]	[3]	[4]	[5]	[6]	[7]	[8]	[9]	[10]	[11]	[12]	[13]	[14]	[15]	[16]	[17]
								30 August 2011				31 August 2011				
#Fibre	ID	RA (°)	Dec (°)	$I-$band (mag.)	distance (kpc)	phot. class.	spec. class.	*SNR*	*hght*	$V_{\rm helio}$ (km s^{-1})	$V_{\rm err}$ (km s^{-1})	*SNR*	*hght*	$V_{\rm helio}$ (km s^{-1})	$V_{\rm err}$ (km s^{-1})	Flag
308	71601	296.34	-14.2	...	5.26	...	...	2	0.22	-35	84	4	0.33	-136	57	...
309	72678	296.37	-14.2	...	5.26	...	...	4	0.27	-128	87	...	...	...	...	...
311	61106	296.33	-14.14	...	5.69	...	...	...	...	...	...	5	0.38	81	77	...
313	193220	296.29	-14.77	19.1	0.53	M	Ce:	7	0.36	-86	87	5	0.46	10	32	C
314	198595	296.26	-14.79	19.7	0.22	M	Ce:	15	0.7	-51	28	12	0.79	-46	24	C
316	162531	296.28	-14.66	...	1.28	...	...	3	0.35	-7	32	4	0.44	-26	38	...
317	29959	296.4	-13.99	...	7.09	M	dM:	6	0.48	-11	35	9	0.51	-53	43	M
318	61790	296.46	-14.15	...	5.9	...	...	5	0.29	-66	53	6	0.51	-48	32	...
319	32087	296.55	-14	...	7.36	M	dK	5	0.29	17	76	10	0.5	88	53	...
320	183545	296.29	-14.74	...	0.68	...	...	9	0.58	-27	34	7	0.69	-43	28	...
321	196632	296.25	-14.79	...	0.16	...	...	17	0.64	-56	46	14	0.72	-117	28	...
322	188333	296.35	-14.76	18.6	1.05	M*	C:	27	0.74	-17	39	12	0.84	-51	19	C
323	174472	296.34	-14.71	19.0	1.17	C*	C	5	0.51	-57	34	7	0.57	-72	29	C
324	67487	296.49	-14.17	...	5.78	M	dM:	6	0.31	30	71	8	0.42	63	54	M
325	170941	296.29	-14.7	19.4	1	M*	dK	14	0.64	-20	42	16	0.66	-47	32	...
326	176863	296.35	-14.72	19.0	1.19	C*	C	7	0.53	-37	27	6	0.51	-62	23	C
327	83584	296.46	-14.26	...	5.03	M	dM:	9	0.34	-18	83	15	0.59	37	34	M
328	187649	296.24	-14.75	18.7	0.41	M	C:	9	0.66	-75	25	11	0.72	-46	18	C
330	167230	296.34	-14.68	20.0	1.33	C*	C	4	0.49	-31	46	7	0.51	-123	41	C
332	35137	296.65	-14.02	...	7.57	M	dK:	5	0.29	-27	116	8	0.27	-76	105	...
334	177839	296.25	-14.72	19.4	0.68	M	C	8	0.63	0	27	9	0.65	-32	28	C
336	38421	296.71	-14.03	...	7.68	M	dK:	...	...	...	...	6	0.28	-23	34	...
337	45220	296.77	-14.07	...	7.68	...	...	...	...	...	...	8	0.3	48	77	...
338	164010	296.33	-14.67	19.1	1.39	M	C	4	0.34	-100	66	7	0.6	-53	20	C
345	117821	296.71	-14.43	...	5.06	...	...	7	0.34	-40	72	...	...	...	...	...
348	80533	296.85	-14.24	...	7.03	...	...	4	0.37	-26	67	...	...	...	...	...
349	176619	296.23	-14.72	...	0.7	...	...	6	0.54	-62	34	9	0.65	-28	25	...
351	98241	296.65	-14.33	...	5.32	M	dM	5	0.52	-138	30	10	0.41	-42	95	M
352	91537	296.61	-14.3	...	5.35	...	...	3	0.44	-107	46	...	...	...	...	...
354	165802	296.41	-14.67	...	1.81	...	...	3	0.26	-12	82	6	0.53	-37	40	...
355	82795	296.95	-14.25	...	7.54	...	...	...	...	...	...	7	0.28	-141	111	...
357	84888	297	-14.26	...	7.81	...	...	3	0.31	-194	34	...	...	...	...	...
358	123455	296.83	-14.46	...	5.71	...	...	...	...	...	...	5	0.42	-48	71	...
359	127636	296.79	-14.49	...	5.31	M	dK:	4	0.29	-14	96	9	0.56	-15	53	...
360	104563	296.96	-14.36	...	7.07	...	...	3	0.43	-197	49	...	...	...	...	...
361	112177	296.82	-14.4	...	5.94	M	dM:	5	0.24	33	66	11	0.5	-4	75	M
362	81011	296.98	-14.24	...	7.81	M	dM	...	...	...	...	8	0.33	74	94	M
364	110475	297.01	-14.39	...	7.28	...	...	3	0.35	-5	90	5	0.4	9	64	...
366	152918	296.81	-14.61	...	5.06	M	C:	4	0.24	82	99	9	0.58	14	26	...
368	119903	296.79	-14.45	...	5.54	...	...	...	...	...	...	7	0.43	-33	85	...
369	167631	296.51	-14.68	...	2.49	...	...	3	0.36	-12	22	...	...	...	...	...
370	140011	296.8	-14.55	...	5.16	M	dM:	6	0.43	28	32	12	0.49	-9	41	M
371	117981	297.05	-14.44	...	7.45	...	...	...	...	...	...	8	0.4	-7	46	...
372	117401	297.1	-14.43	...	7.84	M	dK:	...	...	...	...	6	0.3	57	57	...
373	158905	296.83	-14.64	...	5.09	...	...	3	0.27	150	64	7	0.59	-22	28	...
374	141439	296.83	-14.56	...	5.4	...	...	2	0.49	17	40	5	0.33	18	43	...
375	130447	297.13	-14.5	...	7.86	...	...	2	0.27	163	55	5	0.34	11	40	...
376	148616	296.85	-14.59	...	5.43	M	dK:	...	...	...	...	8	0.28	5	44	...
377	152475	296.85	-14.61	...	5.4	...	...	...	...	...	...	10	0.26	-150	45	...
378	124695	297.06	-14.47	...	7.44	...	...	5	0.24	110	93	9	0.43	75	45	...
379	128222	297.02	-14.49	...	7.06	M	dM:	5	0.35	-40	36	9	0.25	-149	72	M
380	141960	297.05	-14.56	...	7.05	...	...	3	0.34	-178	53	...	...	...	...	...
381	136987	297.06	-14.53	...	7.21	...	...	6	0.3	-11	59	7	0.23	22	47	...
382	168122	296.87	-14.69	...	5.35	...	...	...	...	...	...	8	0.21	18	116	...
383	146932	297.07	-14.58	...	7.19	M	dM:	...	...	...	...	8	0.4	39	43	M

Continued on next page

Appendix A1 (cont.): Individual *fxcor* returns for objects meeting the criteria ($hght \geqslant 0.2$, -200 km s^{-1} $\leqslant V_{\rm helio} \leqslant +200$ km s^{-1}).

[1]	[2]	[3]	[4]	[5]	[6]	[7]	[8]	[9]	[10]	[11]	[12]	[13]	[14]	[15]	[16]	[17]
								30 August 2011				31 August 2011				
#Fibre	ID	RA (°)	Dec (°)	$I-$band (mag.)	distance (kpc)	phot. class.	spec. class.	*SNR*	*hght*	$V_{\rm helio}$ (km s^{-1})	$V_{\rm err}$ (km s^{-1})	*SNR*	*hght*	$V_{\rm helio}$ (km s^{-1})	$V_{\rm err}$ (km s^{-1})	Flag
384	165837	296.92	-14.67	...	5.79	...	...	3	0.27	-96	94	...	...	...	...	...
388	157802	296.91	-14.64	...	5.78	M	dK:	11	0.34	7	51	...	...	...	...	...
389	165036	297.1	-14.67	...	7.28	...	...	...	...	...	...	7	0.25	77	136	...
390	155389	297.11	-14.62	...	7.42	M	dM:	...	...	...	...	14	0.27	-108	81	M
393	159040	297.1	-14.64	...	7.3	...	...	...	...	...	...	6	0.25	78	47	...
394	165107	297.15	-14.67	...	7.65	M	dM:	4	0.29	-139	53	9	0.53	12	28	M
395	170606	296.9	-14.7	...	5.56	...	...	...	...	...	...	5	0.33	21	58	...
398	204144	296.41	-14.81	19.0	1.42	Unid*	C	11	0.73	-43	25	11	0.63	-50	32	C
399	174894	296.85	-14.71	...	5.14	...	...	...	...	...	...	10	0.64	4	43	...

This paper has been typeset from a TEX/LATEX file prepared by the author.